Data availability statement

Data presented in this publication is accessible on:

- Yildiz, A. and Stirling, R.A. 2020. PLEXUS @ NGIF - Field and laboratory measurements. Newcastle University. doi: 10.25405/data.ncl.c.5088419.

All the scripts used in this publication for data analysis and visualisation can be accessed on the corresponding author's Github page

- Yildiz, A. Data analysis and visualisation for lysimeter data github.com/yildizanil/GETE-D-20-00044

Thermo-hydrological behaviour of green infrastructure: a comparative field and laboratory study

Authors:

1. Anil Yildiz, Dr .Sc.

Research associate, National Green Infrastructure Facility, Newcastle University, Newcastle upon Tyne, United Kingdom.

Research associate, School of Engineering, Newcastle University, Newcastle upon Tyne, United Kingdom.

Orcid: 0000-0002-2257-7025

2. Ross A. Stirling, PhD

Lecturer, National Green Infrastructure Facility, Newcastle University, Newcastle upon Tyne, United Kingdom.

Lecturer, School of Engineering, Newcastle University, Newcastle upon Tyne, United Kingdom.

Orcid: 0000-0002-0069-6621

Corresponding author:

anil.yildiz@newcastle.ac.uk

National Green Infrastructure Facility

Urban Sciences Building, NE4 5TG, Newcastle upon Tyne, United Kingdom

Abstract

Heat recovery and dissipation using shallow, buried exchangers are a recognised cost-effective and renewable alternative to using fossil fuels for space heating and cooling. The efficiency of such ground heat exchangers (GHE) is dictated by the bulk thermal properties of the soil. These are heavily influenced by the soil hydrological regime, which is driven by soil–atmosphere interaction. The typically moist substrate profile of Sustainable Drainage Systems (SuDS), which are designed to possess and maintain a high infiltration and storage capacity, have significant potential as a medium for shallow GHEs. An at-scale field setup was commissioned in this study to monitor the thermo-hydrological behaviour of SuDS. Comparable results to laboratory measurements in terms of soil water retention and thermal conductivity dryout curves were obtained. Furthermore, field measurements indicate that the substrate in the field setup remained in the high thermal conductivity range, even under summer conditions. The conductive substrate and saturation conditions prevalent in SuDS presents an attractive opportunity to address our cities' increasing energy demand under a changing climate.

Keywords: Green infrastructure, Ground heat exchangers, Thermal conductivity, Unsaturated soils, Lysimeter, Field testing

1. Introduction

Space heating and cooling accounts for nearly a third of the final energy demand in the 28 member states of European Union (EU), most of which is provided with fossil fuels.[1] The objective of decarbonising the energy supply can be achieved by increasing the share of renewable energy sources to supply either process or space heating and cooling demand. Geothermal energy, of which the full potential is not exploited, has become a mainstream source for renewable energy with the advancement in technology and management.[2]

A ground source heat pump (GSHP) system uses the ground as a heat source or sink to provide heating and cooling. The heat extraction or injection occurs via a ground heat exchanger (GHE), usually a High Density Polyethylene (HDPE) pipe loop.[3] Deep boreholes, facilitated with vertical pipe loops, are used to provide heat exchange at depth, where there is little or no effect of seasonal soil temperature variation.[4] However, these systems require heavy machinery for drilling, which can be prohibitively expensive for small commercial or residential projects. Shallow, closed loop horizontal GHEs are buried in trenches and offer an economical alternative to deep vertical open or closed loops.[5,6] However, dedicating space to build GSHP systems in densely urbanised areas, where the unit price per area is greatest, can be costly and may result in systems being value engineered out of such schemes.

The efficiency of GHEs is directly related to the thermal properties of the soil in which the loop is installed. Soil thermal properties vary depending on mineralogy, density and saturation. Published values of thermal conductivity can be used as a first step in the design of GSHP systems. For example, thermal conductivity from numerous locations in the United Kingdom (UK) can be accessed,[7] and a recent database of thermal conductivities for both rocks and unconsolidated sediments has been published to develop a decision support system, which can be applied to a wider geographical coverage.[8] However, exchanger designs using fixed values of thermal properties obtained from standards, guidelines or soil maps can result in

overestimation of pipe length, compared to designs using site-specific thermal property values.[9] Incorporating the variation in thermal conductivity, shown to be the most crucial parameter in horizontal GHE performance,[10] between soil types further reduces the required loop length.[11] Numerical simulations of a shallow, horizontal slinky-loop GHE with a fixed loop diameter and pitch in three soil types with differing thermal properties yielded a higher thermal performance for soils with higher thermal diffusivity and thermal conductivity.[12] As shallow horizontal GHEs are placed in trenches, which are backfilled usually with one soil type at a certain density, the variation in thermal conductivity is dominated by the degree of saturation of the soil.[11] Therefore, heat exchange efficiency in shallow GHEs varies throughout the year due to the transience of soil thermal conductivity. As bulk soil thermal properties are a function of soil water content, atmospheric conditions heavily influence the efficiency of shallow GHEs, namely precipitation (addition of water) and evapotranspiration (removal of water) via conducive vapour pressure deficit conditions.

Co-locating shallow GHEs and Sustainable Drainage Systems (SuDS) in cities can provide a complimentary increase in the feasibility of both technologies/approaches. The principle hydrological functions of SuDS are to collect, attenuate and divert excess rainwater and surface runoff from potentially overwhelmed sewer/storm-drain networks using natural processes in soil-plant based Green Infrastructure (GI).[13] As such, a SuDS is typically designed to possess and maintain a high infiltration capacity, in which long-term elevated soil water contents may be expected. It is proposed that the relatively wet substrate of SuDS will possess a higher thermal conductivity, making for a more efficient ground heat exchange medium and thereby, increase GSHP performance. Research into this combined functionality is still in its infancy with notable contributions being in the use of pervious paving and swales.[14,15] Elevated temperature increases the drying rate of soil,[16] therefore the water storage capacity of the soil in the combined GHE – SuDS can be restored or maintained in advance of rainfall or runoff

input under space cooling GSHP operation, in which heat is injected to the ground and causes an increase in soil temperature. Furthermore, it is recognised that increasing the temperature of a storm water receiving bioretention system will enhance the remediation of polluted urban runoff, accelerating and prolonging the water quality improvement function of SuDS.[17]

Besides process-based advantages, there are economic benefits to combined SuDS-GHE installations. The construction sector is increasingly subject to statutory obligation in prioritising sustainable drainage techniques in achieving zero impact on flood risk.[18–20] At the same time, the drive to decarbonise heating and cooling, for example in all new-build UK homes by 2025,[21] is leading to a greater incentive to engineer sustainable water-energy duality in the urban environment. These innovative solutions require an improved understanding of the coupled thermo-hydrological phenomena that are fundamental to both GHE and SuDS performance, enabling combined systems that have the potential to add significant mutual value. Green infrastructure is often developed at building-development scale, yet serves the wider urban catchment in which it is placed. Such distributed SuDS networks lend themselves to hosting integrated GSHE loops, ideal for district heating schemes.

This study aims to investigate the potential of SuDS to be used as a medium for shallow GHE in urban areas by monitoring the thermo-hydrological changes in a pilot-scale, heavily-instrumented SuDS feature. The objectives are: To characterise the water retention and thermo-hydrological behaviour of typical SuDS substrate under laboratory conditions; To determine changes in the thermal conductivity and volumetric water content of the soil column under field conditions and; To compare laboratory behaviour with that recorded in the field.

2. Materials & methods

2.1. National Green Infrastructure Facility

The National Green Infrastructure Facility (NGIF) - located in Newcastle-upon-Tyne, United Kingdom - is a living laboratory for research into green infrastructure approaches via at-scale, functional and heavily monitored SuDS. NGIF was founded as part of the United Kingdom Collaboratorium for Research in Infrastructure & Cities (UKCRIC). The outdoor experimental features comprise lysimeters, in–ground bioretention cells and an extreme event swale, all of which are linked by an extensive environmental sensing network.

The lysimeter setup used in this research, shown in Fig. 1, is composed of a stainless-steel cylindrical vessel with a conical bottom to drain and collect the water that infiltrates through the soil column. The diameter of the cylinder is 2000 mm, height at the edges is 1100 mm and 1200 mm at the centre. A tipping bucket flow gauge, calibrated at 75 ml/tip, is connected via a drain pipe to the bottom of the lysimeter to

Fig. 1: Photo of the lysimeter setup showing the weather station and rainfall gauge.

measure the amount of water draining from the soil at any given time. Meteorological parameters, such as air temperature, relative humidity, wind speed and direction, and net radiation, are measured with instruments situated directly above the lysimeter. A rainfall gauge on the lysimeter provides rainfall data. An adjacent enclosure houses multiple dataloggers and a computer to record and upload data in real-time to dedicated servers.

2.2. Soil

A fine sand, consisting of 99% sand and 1% fines, was used in this study, and was classified as a poorly graded sand (SP) according to the Unified Soil Classification (USCS). Mean particle size (d_{50}) was 0.2 mm. Coefficient of uniformity (C_u) and curvature (C_c) were found as 2.4 and 1.2, respectively. Specific gravity was determined as 2.68. The maximum and minimum dry densities were 1.64 Mg/m^3 and 1.36 Mg/m^3, respectively. The optimum moisture content was determined as 16%. The saturated hydraulic conductivity was determined according to the falling head technique on a sample prepared at a dry density of 1.43 Mg/m^3 in a 250-ml ring using a KSAT device from Meter Group.[22] The mean saturated hydraulic conductivity was found to be 1.73 x 10^{-4} m/s (N=3). This satisfies all minimum recommended values and exceeds only four maximum values provided by six international guidance documents.[13,23–27]

An organic rich substrate, complying with BS3882:2015 standards, was used as topsoil in this study. It consists of 3.3% gravel, 86.3% sand and 10.4% fines, and its specific gravity is 2.41. Carbon:nitrogen ratio was provided as 12:1, and loss-on-ignition technique yielded and organic matter content of 3.4%.[28]

2.3.Test setup

Construction and commissioning of the lysimeter setup, including instrumentation, took place between 10.04.2019 and 02.05.2019. In order to enable free drainage, the conical bottom of the lysimeter was filled with gravel to leave a clear height of 1000 mm. A nonwoven geotextile was laid above the gravel to prevent the migration of fines mitigate blocking of the drain. A double-walled HDPE pipe was placed in the lysimeter to insulate the soil column from the stainless-steel cylinder. The height of the pipe was 1000 mm and the inner diameter was 1800 mm with a wall thickness of 80 mm. A 950-mm high soil column was built up within the pipe, consisting of an 800-mm thick sand layer topped with 150 mm of topsoil.

A target gravimetric water content and relative density chosen for the sand layer was 16% - optimum water content of the sand - and 35%, respectively, resulting in a bulk density of 1.68 Mg/m^3 and a dry density of 1.45 Mg/m^3. Targeted bulk density was chosen to comply with the suggestions of Department for Environment, Food and Rural Affairs (DEFRA) not to impede root growth.[29] The in-situ gravimetric water content of the sand was determined to be between 6% and 7%. Sand was mixed in batches using a cement mixer in order to achieve the target gravimetric water content of 16%. Approximately 428 kg of wetted sand was placed in the pipe for every 100-mm-thick layer, and compaction was performed using a hammer with a weight of 6 kg, until the desired height in the HDPE pipe was reached. Core-cutter density measurements were taken after compaction at each layer, this established a mean bulk density of 1.67 Mg/m^3 at an average gravimetric water content of 16.6%. Standard deviations for bulk and dry densities as well as gravimetric water content were found as 0.05 and 0.04 Mg/m^3, and 1.7%, respectively. Therefore, it was assumed that the target relative density was reached throughout.

Topsoil was placed directly above the sand column, and no compaction was applied so as not to hinder plant growth. The total mass of the 150 mm thick topsoil layer was 460 kg, which gives an overall bulk density of 1.20 Mg/m^3. Topsoil was seeded with *Secale cereale*, which was shown to be suitable for the establishment of meadow vegetation from seeds on bare soil in urban areas.[30] Evidences of using genus *Secale* in a context of GI in bioretention planters to retain stormwater and reduce nickel, copper, zinc and polycyclic aromatic hydrocarbons also can be found in the literature.[31]

2.4. Laboratory testing

2.4.1. Soil water retention curve

The Soil Water Retention Curve (SWRC) was obtained using a HYPROP setup,[32] which consists of a high precision balance and two tensiometers. Change in mass, assuming that it

occurs only due to evaporation, is reflected as a change in water content. As the sample volume is known, it is possible to express a SWRC using either gravimetric (w) or volumetric (θ) water content vs. matric suction (ψ).

The 50-mm-high samples are prepared in 250-ml sample rings, and saturated from below prior to testing. Three samples of sand at dry densities of 1.36, 1.43 and 1.63 Mg/m^3 were tested from a saturated state, another sample of sand at a dry density of 1.43 Mg/m^3 and 16.6% initial water content was prepared to obtain a scanning curve that was representative of the lysimeter condition at the time of commissioning.

2.4.2. Thermal conductivity dryout curve

A sample of sand was prepared at the dry density corresponding to the average value in the lysimeter, and placed on the HYPROP setup while measuring the thermal properties with a KD2 Pro Thermal Properties Analyser from Decagon Devices.[33] A dual-needle sensor was used where thermal properties are estimated based on the response of the soil. The KD2 has a range between 0.02 and 2.00 W/mK, with an accuracy of 10%. Saturated sample was left to evaporate, while volumetric water content and matric suction measurements are performed by the HYPROP setup, and thermal conductivity measurements are taken by the KD2.

Proposed models from the literature that estimate thermal conductivity have been used in this study to compare the calculated and measured values. Equation 1 was put forward to model the thermal conductivity of soils,[34] which uses the thermal conductivity at dry state (λ_{dry}), at saturated state (λ_{sat}) and Kersten function (K_e).

$$\lambda = \left(\lambda_{sat} - \lambda_{dry}\right)K_e + \lambda_{dry} \tag{1}$$

As the soil is formed of soil solids and water in a fully saturated state, λ_{sat} is calculated by using the thermal conductivities of the solids (λ_s) and water (λ_w), and porosity (n)[34] as shown in Eq. 2.

$$\lambda_{sat} = \lambda_s{}^{1-n}\lambda_w{}^n \tag{2}$$

The mineral composition of the fine sand used in this study is unknown. An estimation method has been used to obtain the volume fraction of quartz (q) from mass fractions of sand and silt, as suggested by Tarnawski and Leong[35] in the absence of mineralogy data. A sand fraction of 99% and a silt fraction of 1% provides a q of 0.84, therefore λ_s can be calculated[36] as shown in Eq. 3, while λ_w can be taken as 0.594 W/mK.[37]

$$\lambda_s = 2.00^{(1-q)}7.70^q \qquad \text{where} \quad q > 0.2 \tag{3}$$

Equation 3 uses two values for the thermal conductivity of the soil forming minerals. The value for quartz is 7.70 W/mK,[38] and an average value of 2.00 W/mK was used for other minerals, e.g. kaolinite, calcite, illite,[36] Zhang et al.[36] compared numerous available methods for estimating λ_{dry} and K_e and concluded that the He et al.[39] model for λ_{dry} and the Côté and Konrad model (CKM),[40] based on degree of saturation (S_r), for K_e performed best. Eqs. 4 and 5 show the formulas used to estimate λ_{dry} and K_e, respectively. The CKM uses an empirical factor, k, which was defined as 3.55 for medium and fine sands.

$$\lambda_{dry} = -1.92n + 1.18 \tag{4}$$

$$K_e = \frac{kS_r}{1 + (k-1)S_r} \tag{5}$$

A range of S_r from 0.00 to 1.00, in increments of 0.01, was used in Eq. 5, which are converted into θ using the specific gravity of the sand and void ratio corresponding to mean dry density of the sand in the soil column.

2.5. Field instrumentation

5TE sensors from Decagon Devices[41] were used to estimate θ from measurements of dielectric permittivity. The accuracy of these sensors using factory calibration is ± 3.0 %. MPS-6 sensors from the same company were used to monitor ψ in the soil. These sensors consist of a porous ceramic disc, for which the water retention curve is well defined. Water content of the ceramic disc is estimated based on the measurement of the dielectric permittivity and then converted into ψ .[41] The measurement range is given as -9 to -100,000 kPa and an accuracy of ± 10% plus 2 kPa. Both sensors also have the ability to measure soil temperature with an accuracy of $\pm 1°C$.

Table 1 shows the location of the sensors in the soil column, each sensor was placed horizontally at 200 mm away from the vertical centre line at radial angles defined in Table 1. Locations were chosen to minimise sensor interference, and have representative values at each depth. A spatial average value of matric suction and volumetric water content is obtained by taking the mean of readings from both sensors, and temporal average values are calculated every 15 minutes. A running median with a window of 5 has been used to eliminate isolated outliers.

Table 1: Locations of sensors used for measuring volumetric water content and matric suction. Values given show the radial angles they were placed.

Depth [mm]	Volumetric water content	Matric suction
100	0, 90	180, 270
250	45, 135	225, 315
350	90, 180	270, 360
450	135, 225	315, 45
550	180, 270	0, 90
650	225, 315	45, 135
750	270, 360	90, 180

Thermal conductivity is measured at 250, 350, 550 and 750 mm depth with TP01 sensors from Hukseflux.[42] Operating range of this sensor is between 0.3 and 4.0 W/mK, with an accuracy of ± 10%. The TP01 sensor measures the radial temperature difference around a

heating wire with 2 thermopiles. Voltage is supplied every 3 hours for 3 minutes to the heating wire in the sensor, and a voltage difference is generated as a response to heating.[42] Measurements every 3 hours are used individually to monitor the variation of thermal conductivity as a result of change in soil water content. In addition to the temperature measurements provided by 5TE and MPS6 sensors, a Hukseflux STP01 soil temperature profiler was placed 50 mm below the surface, providing readings at 70, 100, 150, 250, and 550 mm. Campbell Scientific TCAV, averaging soil thermocouple probe, was used to estimate an average temperature at 40 mm below the surface. Two Campbell Scientific 107 thermistors were used at 800, 840-850 and 900 mm.
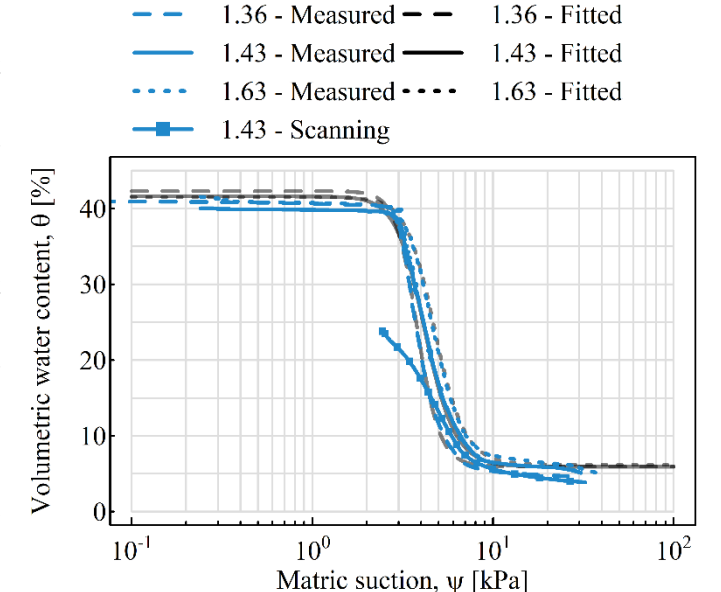
3. Results

All data from the monitored lysimeter setup presented is openly accessible via the Newcastle University data repository.[43] All the scripts used in data analysis and visualisation are also accessible.[44]

3.1. Laboratory testing

3.1.1. Soil water retention curve

Figure 2 presents the SWRC for three samples of the sand used in the lysimeter. A non-linear least square algorithm was used to fit the van Genuchten SWRC equation[45] to the measured data of the samples tested at the minimum and maximum dry densities, as well as at the average density of the sand in the lysimeter.

Fitting parameters for each curve are presented in Table 2. A slight decrease in the saturated water content (θ_s) can be seen with increasing dry density, but there were no significant differences in the residual water content (θ_r). The more loosely packed sample had a lower air entry value, which increases with increasing dry density. Denser samples experienced higher matric suction at the same θ in the

Fig. 2: Soil water retention curve of the sand used in the lysimeter. Numeric values shown in the legend indicate the dry densities of the samples tested in Mg/m³.

funicular phase of drying, i.e. intermediate values of saturation. A scanning curve is also illustrated in Fig. 2, which starts from an initial w of 16.6%, mean gravimetric water content at time of placement into lysimeter, and ends with a curve lying below the other SWRCs.

Table 2: Fitting parameters of van Genuchten (1980) equation to the measured data in the laboratory.
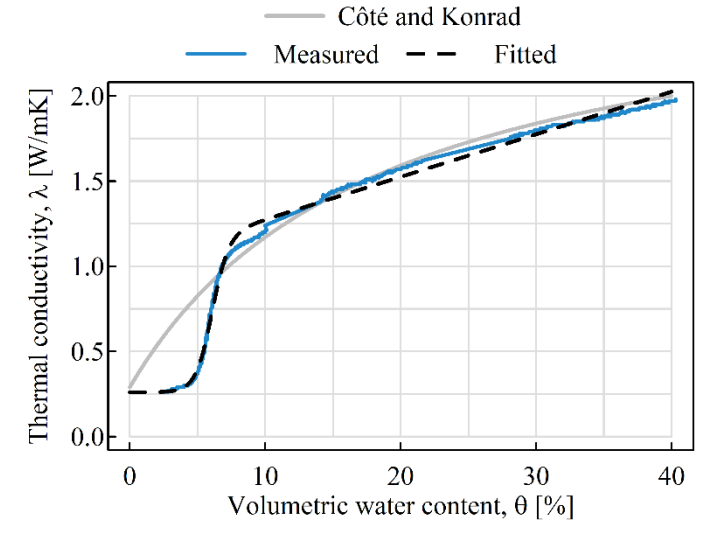
Dry density [Mg/m³]	θ_s	θ_r	α	n
1.36	42.3	5.94	0.27	7.42
1.43	41.6	5.92	0.25	5.64
1.63	41.5	6.19	0.22	5.72

3.1.2. Thermal conductivity dryout curve

Figure 3 illustrates the TCDC measured in the laboratory at 1.43 Mg/m³, the mean dry density of sand in the lysimeter. Three visible regimes can be identified in the measured TCDC. No significant change in the thermal conductivity ($\lambda \sim 0.26$ W/mK) is visible in the first regime at the dry end of the TCDC ($\theta < 4.0\%$). A steep increase with increasing volumetric water content is observed in the second regime ($4.0\% < \theta < 8.0\%$), followed by a gradual increase towards the wet end of the TCDC ($\theta > 8.0\%$). Due to the trend shown in the experimental data, a modified sigmoid curve is fitted to the measured data using Eq. 6 and a non-linear least square algorithm in R 3.6.1. Modification consists of adding a term to define the gradual increase after the first steep increase.[46]

$$\lambda = 0.261 + \frac{0.915 + 0.025(\theta - 6.04)}{1 + e^{-1.65(\theta - 6.04)}} \tag{6}$$

Figure 3 shows the CKM in addition to the fitted TCDC based on Eq. 6. Porosity was substituted into Eq. 4 to estimate λ_{dry} as 0.29 W/mK. Equation 3 yields a λ_s value of 6.21 W/mK using a quartz content of 0.84,[35] and substituting this value into Eq. 2 gives a λ_{sat} of 2.08 W/mK. It can be seen that λ_{sat} and λ_{dry} from Eqs. 4 and 6,
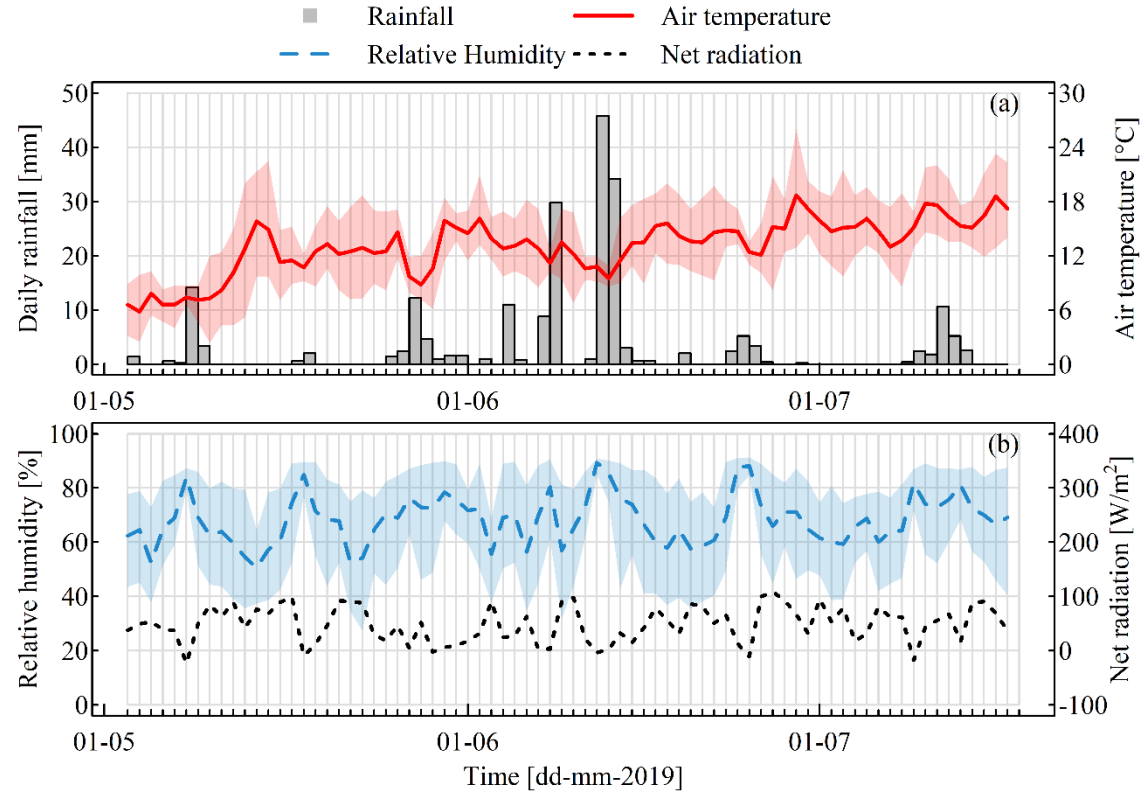

Fig. 3: Thermal conductivity dryout curve (TCDC) of a reconstituted sand sample.

respectively, are in agreement with the laboratory measurements. The goodness-of-the-fit is evaluated between these two models by comparing the root mean square error (RMSE). CKM provided an RMSE of 0.27, whereas the one of the fitted equation was 0.035.

3.2. Field testing

Results from the field monitoring cover the period from 03.05.2019 00:00 to 18.07.2019 00:00. All times are given in Coordinated Universal Time (UTC).

Fig. 4: (a) Daily total rainfall and air temperature, and (b) relative humidity and daily net radiation during the period of monitoring. Shaded areas in the figures show the extent of daily measurements, i.e. the minimum and maximum values in a day.
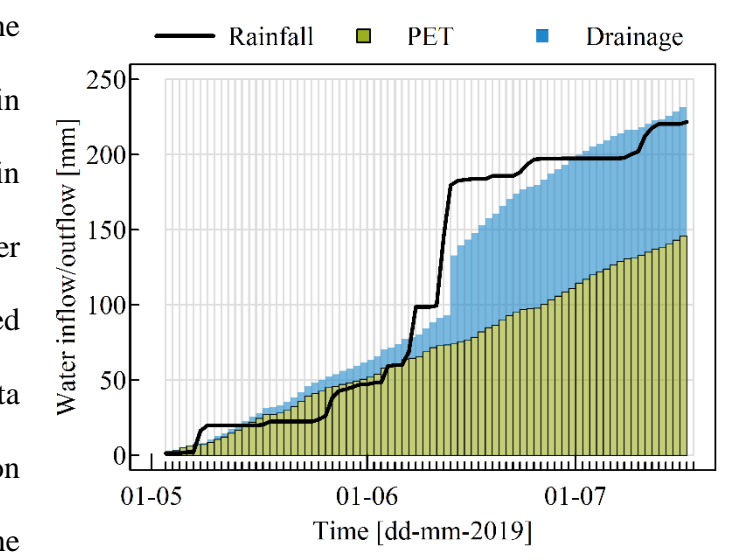
3.2.1. Meteorological measurements

Figure 4 illustrates the amount of daily rainfall, total precipitation from 00:00:00 to 23:59:59. The daily minimum and maximum recorded air temperature, as well as daily mean values are also presented. The field monitoring presented herein covers a period of 76 days, of which 36 days had precipitation, i.e. daily total rainfall more than 0.2 mm. The total precipitation during monitoring was calculated as 221.8 mm with a maximum daily total rainfall

of 45.8 mm. Air temperature data shows an upward trend through this period with a maximum and minimum recorded air temperature of 26.0 °C and 2.40 °C, respectively.

Daily mean relative humidity ranged between 50.6 % and 89.3 %, with lowest recorded value of 27.3% and the highest at 91.3%. Daily mean net radiation values were between -23.2 W/m^2 and 108.6 W/m^2. Relative humidity was positively correlated with daily total rainfall (R^2 = 0.29, $p < 0.001$) and negatively correlated with daily net radiation (R^2 = 0.43, $p < 0.001$). The immediate effect of the changes in relative humidity and net radiation is reflected on the daily *PET*. Lower relative humidity (R^2 = 0.58, $p < 0.001$) and higher mean net radiation (R^2 = 0.77, $p < 0.001$) resulted in higher values of *PET*.
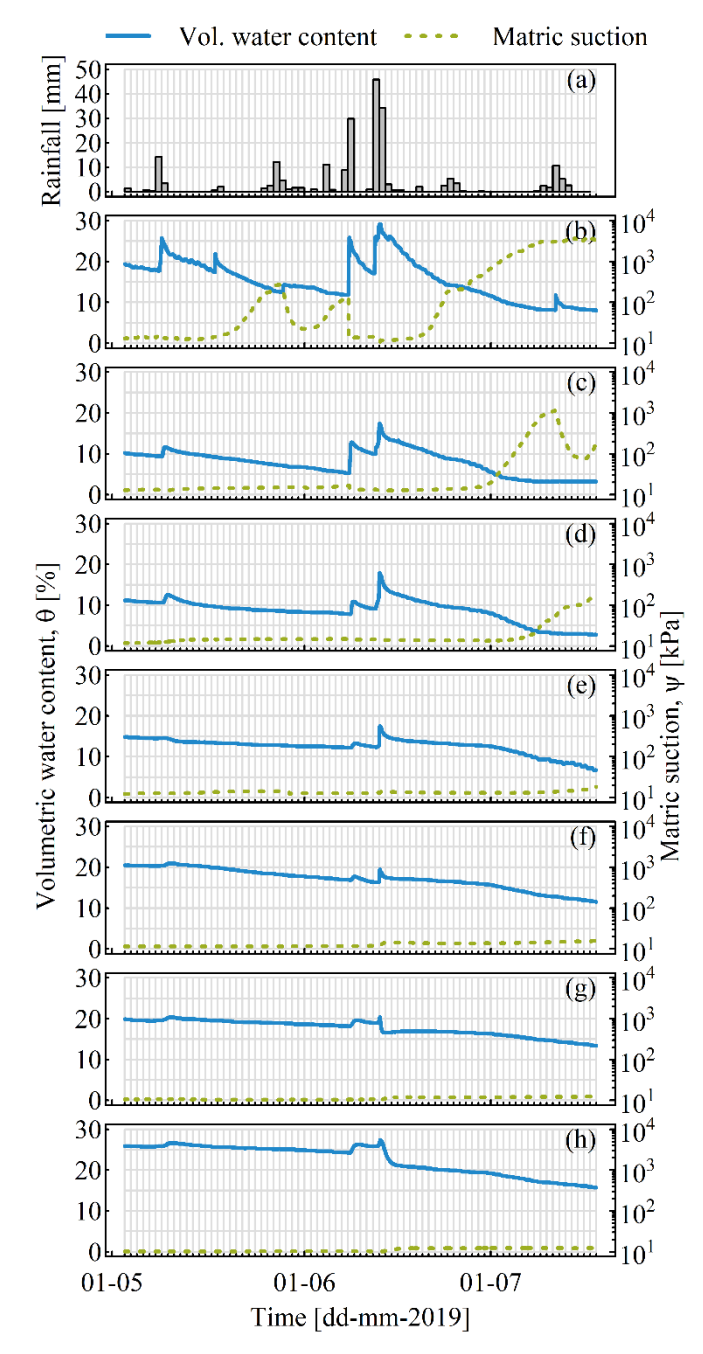
3.2.2. Hydrological measurements

The hydrological regime of the lysimeter has been investigated in terms of water balance and changes in θ and ψ. Figure 5 illustrates the water balance terms for the whole monitored period. The daily meteorological data recorded by the weather station situated above the lysimeter and the soil heat flux measurements below the surface have been used to calculate the

Fig. 5: Lysimeter water balance. Water losses comprise potential evapotranspiration and drainage while rainfall represents water input.

potential evapotranspiration (*PET*) using the FAO Penman – Monteith method.[47] Loss of water from the system in form of evapotranspiration and drainage has been summed up to compare with the input of water by precipitation. Daily *PET* ranged between 0.10 and 3.91 mm, and the total value was 148.5 mm. The total drainage was calculated as 85.5 mm, most of which occurred after 13.06.2019.

As two distinctly different types of soil were used in the column, topsoil and sand, different hydrological regimes were monitored (See Fig. 6). Volumetric water content measurements in the topsoil at 100 mm depth respond most clearly to the rainfall events. At the beginning of the monitoring period, θ starts around 20%, reaching a maximum value of 29.2% coincident with an intense rainfall event before decreasing subsequently to 8% by the end. A general increase in sand θ with increasing depth is evident. A decrease in θ after the heavy rainfall between 12.06.2019 and 14.06.2019 can be seen in the soil column at all depths, which corresponds with generation of significant values of ψ in the topsoil and the shallow sand layers.
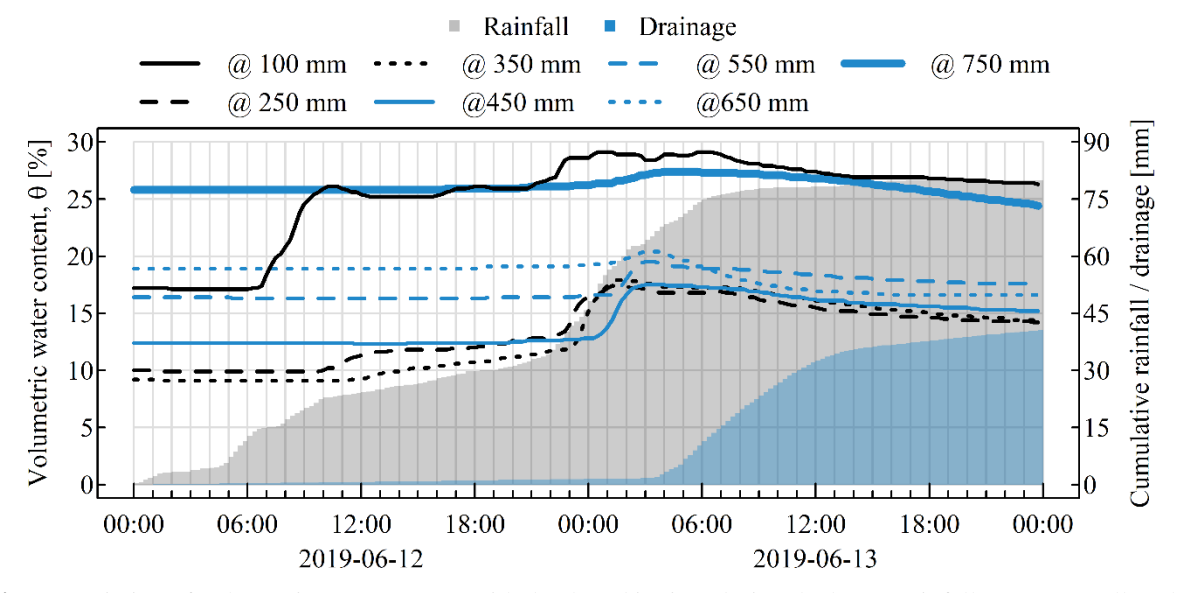

Fig. 6: (a) Daily total rainfall, and variation of volumetric water content and matric suction in time at (b) 100, (c) 250, (d) 350, (e) 450, (f) 550, (g) 650 and (h) 750 mm.

No matric suction measurable with an MPS-6 sensor ($\psi < 15 - 20$ kPa) was generated throughout the monitoring period below a depth of 350 mm.

Figure 7 shows the response of the soil column to the aforementioned heavy rainfall. No change in θ at all depths was observed between 12.06.2019 00:00 and 06:30 until a cumulative rainfall of 14.6 mm was reached. An increase in θ at 100 mm can be seen at 12.06.2019 06:30,
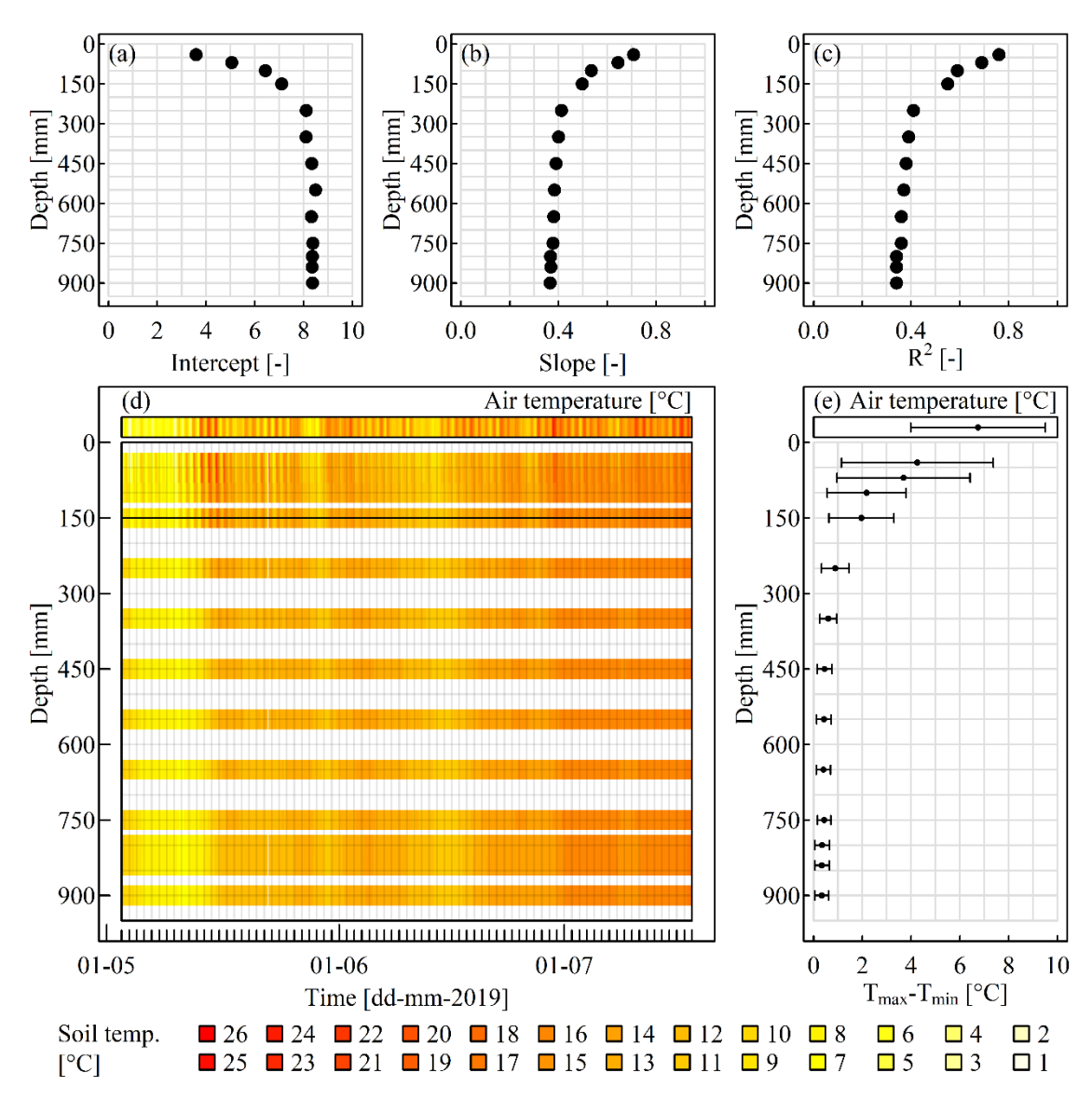
whereas θ starts increasing at 250 and 350 mm after 10:15 and 11:30, respectively. Sensors at depths below 450 mm indicated an increase in θ shortly after 13.06.2019 00:00 with a delayed response for deeper layers. The amount of water draining from the bottom of the lysimeter increases abruptly after 13.06.2019 03:30, which corresponds to the initiation of a gradual decrease in θ at all depths. The greatest response range is observed at the shallowest measurement at 100 mm, whereas a very minor change can be observed in the measurements at 750 mm. The final θ values at 13.06.2019 23:59 are higher than the initial values at 12.06.2019 00:01, except at the lowest depths, 650 and 750 mm.

Fig. 7: Variation of volumetric water content with depth and in time during the heavy rainfall event, as well as the cumulative rainfall and drainage.

3.2.3. Thermal measurements

In order to investigate the effects of air temperature on the soil temperature in the lysimeter setup, linear regressions have been performed. Figures 8a and 8b show how the intercept and the slope of the regression changes with depth, while Fig. 8c illustrates the R^2 value of the regressions. An increase in the intercept of the regression, but a decrease in its slope, is evident with increasing depth, but very minor changes can be observed for layers deeper than 250 mm. Mean value of the intercept and regressions for these layers are 8.3 and 0.38, respectively. A lower R^2 can be seen with increasing depth, starting from 0.76 for the
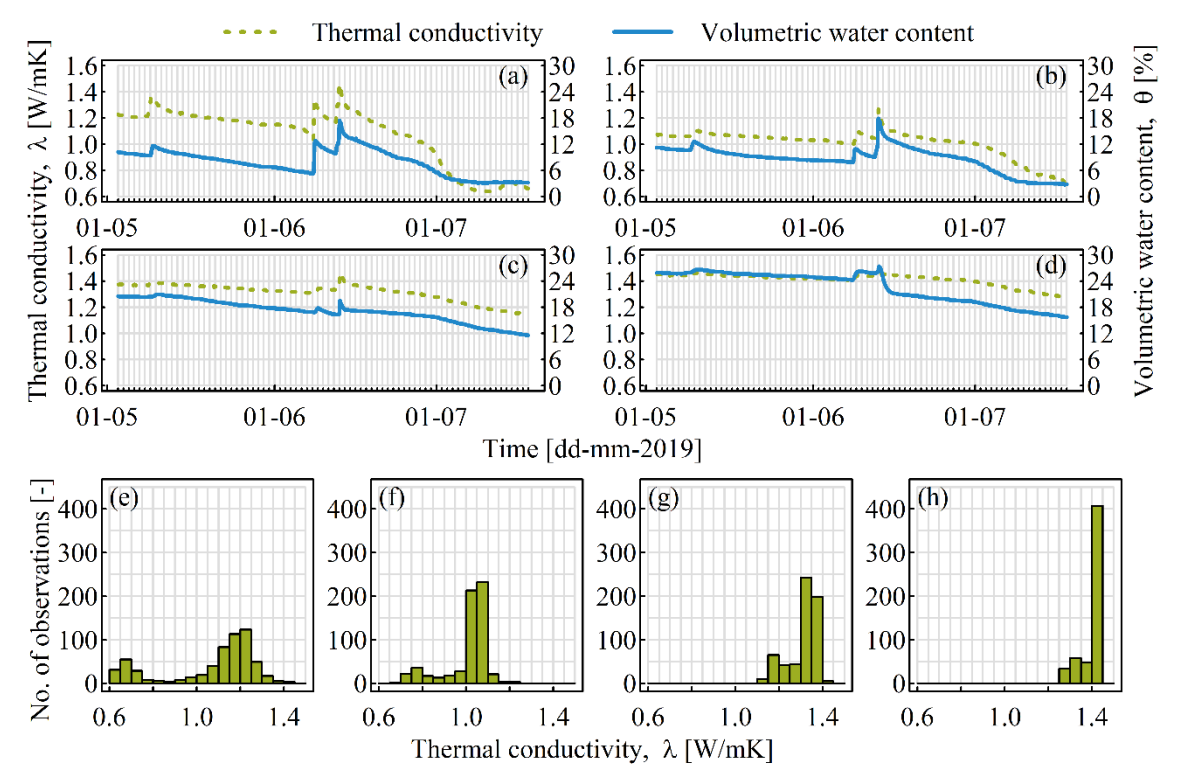
Fig. 8: (a) Intercept, (b) slope and (c) R^2 value of the linear regressions performed between the air temperature and soil temperature at different depths. Temperature values are depicted as a contour plot in (d) to illustrate the variation with depth and time. Mean values of difference between maximum (T_{max}) and minimum (T_{min}) temperature in a day is given in (e). Error bars in (e) show ± standard deviation.

shallowest measurements at 40 mm with TCAV and decreasing to 0.34 for the deepest measurements at 900 mm with Campbell 107 thermistors. A contour plot presented in Fig. 8d shows the change in soil temperature with depth and in time. Diurnal cycles of air temperature are clearly identifiable, which are reflected also at depths less than 250 mm. Figure 8e presents the mean and standard deviation values of the difference between the maximum and minimum temperature in a day. Mean difference in a day at 40 mm was 4.3 °C with a standard deviation

of 3.1 °C, whereas it was 0.33 °C at 900 mm, with a standard deviation of 0.29 °C. Similar trend of minimal change after 250 mm depth can also be observed in Fig. 8e.

Figures 9a – 9d illustrate the variation of λ and θ in the sand layer at 250, 350, 550 and 750 mm. A general reduction in both parameters are evident in the figures at all depths over the period of monitoring. Changes in θ due to rainfall, as presented in Section 3.2.2 and Fig. 6, are reflected as changes in λ. The heavy rainfall event between 12.06.2019 and 14.06.2019 causes an abrupt increase in both parameters, which decreases gradually thereafter, except at 750 mm, where a relatively rapid reduction in θ is visible but a much slower reduction in λ.
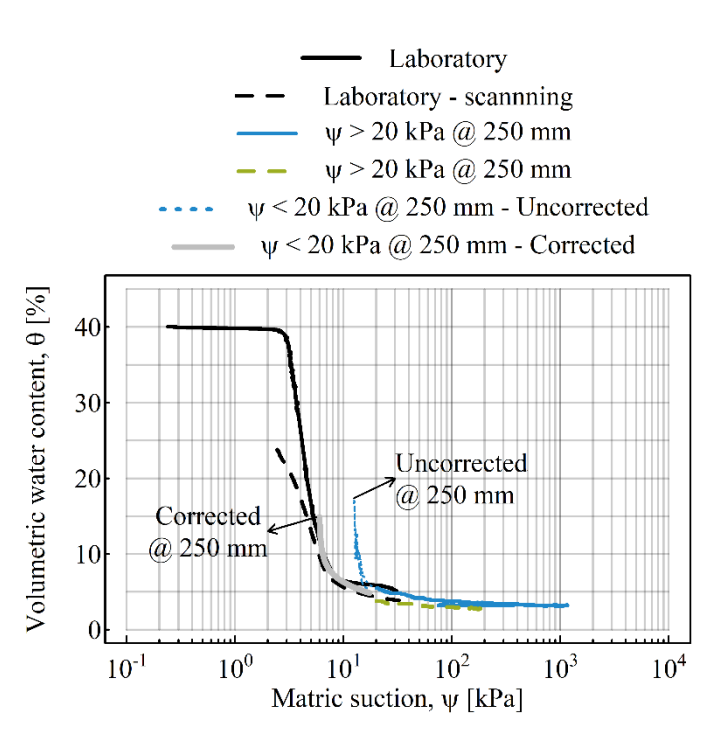

Fig. 9: Variation of thermal conductivity and volumetric water content measured at (a) 250 mm, (b) 350 mm, (c) 550 mm and (d) 750 mm. Subfigures (e) to (h) show the frequency distributions for the same depths.

There is an increase in mean θ with depth, which can also be observed in λ. The values of λ at all depths ranged between 0.64 and 1.47 W/mK, while the mean values were between 1.01 and 1.41, showing an increase with depth. Figs. 9e – 9h present the frequency distributions of the λ measurements, all of which show a left-skewed distribution.

3.3. Laboratory vs. Field Measurements

Comparison of laboratory and field measurements is made in terms of SWRC and TCDC. Figure 10 shows $\theta - \psi$ measured in the laboratory on two samples with a dry density of 1.43 Mg/m³. The black solid line shows data from a saturated sample, whereas the black dashed line is from a sample prepared at the initial mean water content of the sand used in the lysimeter. The scanning curve starts at a w of 16.6% and a θ of 23.7%, and
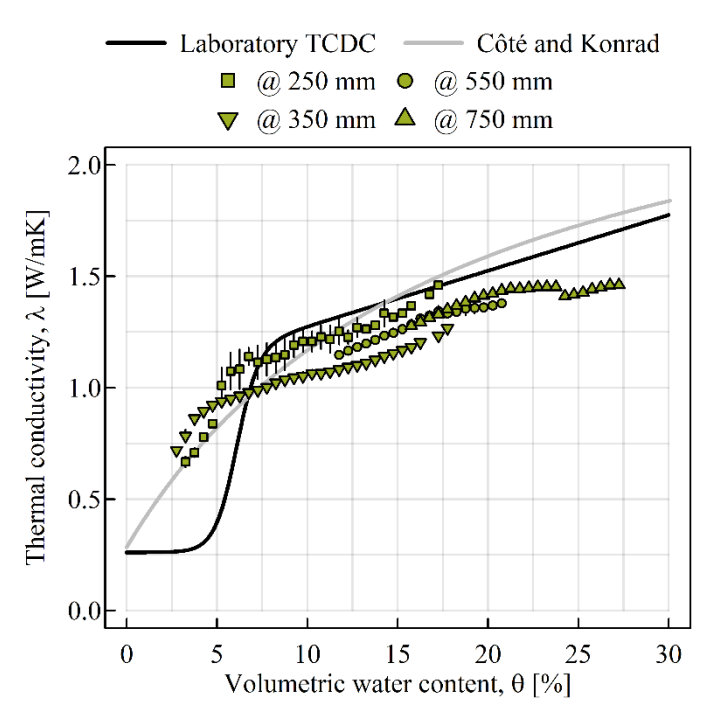

Fig. 10: Laboratory vs. field soil water retention curves of sand used in this study, as well as out-of-range reading correction for MPS-6 sensors at 250 mm based on laboratory measurements.

lies below the curve of the saturated sample. Measurements in the sand layer of the lysimeter at 250 mm and 350 mm are in agreement, and complement the laboratory curves. However, due to the measurement range of MPS-6 sensors, only the dry end of the SWRC could be captured in the field.

As the wet end of the laboratory-derived SWRC and the dry end from the field tally, readings of θ corresponding to ψ values less than 20 kPa are used to estimate corrected ψ values via the inverse of the van Genuchten[45] equation. Figure 10 shows also an example of a corrected field ψ measurement at 250 mm. The minimum reading given by the suction sensors at 250 mm was 12.5 kPa. Values of θ used in the correction equation ranged between 5.28 and 17.7%. Correcting the suction readings completed the SWRC, with suction values reaching to as low as 4.9 kPa.

The solid grey line in Fig. 11 illustrates the TCDC obtained by using CKM and the solid black line is the fitted laboratory TCDC, defined by Eq. 6. The fitted TCDC and CKM differ significantly only in the pendular region (dry end) of the curve, and follow a similar trend for θ values higher than 15%. Field measurements of λ are grouped into 0.5% steps of θ, and mean values as well as standard deviations are plotted in Fig. 11. Field

Fig. 11: Comparison of thermal conductivity and volumetric water content measurements from the laboratory, field and literature. Error bars show ± standard deviation.

measurements show some scatter, but are concentrated around the funicular phase of the soil, with only measurements from 250 and 350 mm moving into the pendular state. The scatter is less evident in the measurements from 550 and 750 mm.

4. Discussion

Evaporation is the main source of water loss from the lysimeter (See Fig. 5), except for the period during and subsequent to heavy rainfall between 12.06.2019 and 14.06.2019 (See Fig. 7). The water balance estimation, as illustrated in Fig. 5, does not include the canopy interception, which can amount to between 5% and even up to 38% of the gross precipitation for genera *Secale*.[48,49] Excluding canopy interception from the water balance, Figure 5 suggests that marginally more water was lost by the end of the monitoring period than was input by rainfall, i.e. water content at all depths were lower than the initial values on 03.05.2019. Comparing the water balance (See Fig. 5) with soil water content and matric suction measurements (See Figs. 6b to 6h) also shows that periods with a negative water balance, when

the cumulative drainage and *PET* exceeds cumulative rainfall, match with the drying of the soil column, and vice versa. Furthermore, rapidly increased drainage subsequent to the heavy rainfall can be an indicator of the sand having reached field capacity, and drainage under gravity dictating changes in the water content.[50] This is also reflected in the volumetric water content at 750 mm, which was the highest value observed at all depths shortly before the drainage event (See Figs. 6b to 6h and 7). The dynamic hydrological regime results in highly fluctuating suction generation and thermal behaviour.

The SWRC defines the water retention capacity and conductivity of the soil,[45] and it is therefore crucial to obtain a full SWRC to be able to assess the performance of SuDS under the entire range of climatic conditions. A reduction in the saturated volumetric water content with increasing dry density was observed in the laboratory-determined SWRCs (See Table 2), which was also shown by Chen[51] on silty sand. A change in dry density of the sample affected the slope of the SWRC at the intermediate saturation values, but not the residual water content (See Fig. 2). Even with the extended capacity of the tensiometers used in the HYPROP setup,[52] only the wet end of the SWRC could be obtained in the laboratory.

Dielectric permittivity-based sensors, such as the MPS-6 from Decagon Devices, provide accurate measurements within a limited range,[53] but they suffer from an inability to accurately measure the wet end of the SWRC. As the range of the MPS-6 starts from 9 kPa, with an accuracy of 10% of the reading with an additional 2 kPa, the sensor is not able to provide reliable readings below 15 to 20 kPa. As the air entry value of the sand used in this study is 3 kPa (See Fig. 2), it is hard to comment on the saturation of the sand column because it is not in the reliably measurable range of the suction sensor. However, these sensors are useful in providing the dry end of the SWRC.[54] Combining laboratory-determined SWRCs of the sand used in this study (See Fig. 2) and the field-determined SWRC (See Fig. 9) presents the full range of SWRC.

Three regimes on an SWRC are defined: capillary (quasi-saturated), funicular (intermediate saturation) and pendular (low saturation),[55] which has also been applied to the concept of TCDC. Separation of these zones were mostly done visually.[55–57] however, the use of a modified sigmoid curve (See Eq. 6 and Fig. 3) removes the need to define the regimes visually, and can define the entire range of TCDC mathematically.[46]

A link between thermo-hydrological parameters in the field can be established by comparing the presented hydrological changes to the measurements of thermal conductivity made in the lysimeter (See Fig. 9). As the thermal conductivity is a function of water content,[34] an increase in water content due to rainfall resulted in an increase in thermal conductivity, and similarly, drying periods correspond to reductions in measured thermal conductivity at all depths. The rate of reduction in the thermal conductivity during drying changed according to the degree of saturation of the soil. When near saturation conditions are reached, referred to as the superfluous domain,[58] and drainage occurs, thermal conductivity stays constant or decreases slowly.[6] This can be seen in Fig. 9d, where θ reaches to its maximum value after the heavy rainfall and drainage occurs while λ is decreasing gradually in time.

Figure 11 compares the TCDC obtained using an empirical model from the literature, measured $\lambda - \theta$ data from various depths in the sand layer of the lysimeter as well as the fitted, laboratory-determined TCDC. It can be noted that the majority of the field measurements are concentrated around the intermediate saturation values, which shows an agreement with both fitted TCDC from the laboratory and the CKM. The scatter of the field data is highest at shallow depths, 250 and 350 mm, which have higher numbers of drying – wetting cycles compared to the more slowly changing hydrological regime at 550 and 750 mm depths. Erroneous matching of a parameter, thermal conductivity in this study, to a particular water content can happen especially in rapidly changing environments.[59] As the number and magnitude of wetting and drying events are higher at shallow depths, the likelihood of such a matching also increases.

There are temperature differences between layers of sand (See Fig. 8), which could have affected the measured thermal conductivity. Nikolaev et al.[60] showed that temperature-driven change in thermal conductivity was prominent for soil temperatures higher than 40 °C. As the maximum soil temperature in the soil column is less than 26 °C, temperature effects were not considered significant in this study.

There are two main sources of discrepancy between the field measurements and laboratory measurements of λ. Firstly, in the funicular state the laboratory-derived TCDC shows higher values than the field measurements for a given volumetric water content.

The laboratory λ was determined using a KD2, whereas field measurements were made with TP01 sensors. No direct comparison between two sensors was conducted in this study, however other researchers have provided evidence that the TP01 typically produces lower values of λ compared to the KD2.[9]

Secondly, both field and fitted laboratory TCDCs for the sand used in this study follow a similar trend, but the point at which λ starts decreasing differs significantly between the measurements from the field and the laboratory. This inflection point corresponds to a volumetric water content of 8% from the fitted laboratory TCDC, whereas it occurs around 5% in the field (See Fig. 11). This is due to the difference in the water content of the sample for which the TCDC was determined in the laboratory and the water content at which the thermal conductivity is measured with dual needles. The evaporation technique used to determine continuous TCDCs in the laboratory introduces a variation between the field-determined and laboratory-determined TCDCs. A 50-mm high sample was used to measure thermal conductivity with 30-mm-long needles inserted to the top of the sample; however, the volumetric water content is estimated for the whole sample via change in mass. As evaporation occurs only from the top surface, a water content gradient is expected, i.e. thermal conductivity is measured at a point where volumetric water content may be lower than the sample mean.

Dong et al.[61] showed, using a similar setup, that various TCDCs can be obtained for the same sample depending on the point of measurement in the sample.

The fitted laboratory TCDC and the CKM are in agreement for the wet end, ($\theta > 15\%$), although discrepancy is shown at the dry side of the TCDC. Overestimation of λ at low water contents is a recognised limitation of the CKM,[37] which results from K_e increasing linearly with S_r. However, little or no increase in λ has been observed at low water contents[55,62] due to the occurrence of heat conduction through grain-to-grain contacts and air,[63] which was also documented from the laboratory measurements in this study. Transition from the funicular state to pendular state occurs at a critical water content,[55] which coincides with the first formation of continuous water bridges.[63] This results in a sharp increase of λ with increasing θ. Therefore the model presented here is considered as the best representation of the measured TCDC.

The specification of appropriate SuDS substrates is a much discussed topic among green infrastructure researchers and practitioners alike and is typically tailored to site-specific function priorities, e.g. water attenuation, storage and/or treatment *in situ*, among others. There exist regional and national level guidance documents that principally provide recommendations regarding particle size distribution and saturated hydraulic conductivity ranges and limits.[13,23–27] At present these are aimed at meeting the hydrological needs of SuDS; however, with the opportunity to add value to installations, such as ground heat exchange for renewable energy, thermal properties of substrates must also be considered. It is important to note that optimising SuDS substrates for thermal behaviour should not necessarily compromise hydrological performance. Furthermore, it was shown that even though air temperature caused a change in soil temperature at all depths, its effects were less critical for deeper layers. Linear regressions presented in Figs.8a-8c and the daily temperature difference given in Fig. 8e yield that diurnal changes of soil temperature occurred mostly at shallow layers, but there is a long-term effect of air temperature on the soil temperature for deeper layers.

Typical GSHE designs rely on constant thermal property values derived from soil property maps or 'snap-shot' site tests, this can be improved further by use of the TCDC. Simulations of Wu et al. (2015) showed that using the TCDC rather than a conservative and constant value of thermal conductivity resulted in 25 to 50% shorter loops.[11] This becomes yet more pertinent given the highly transient saturation conditions typical in SuDS. Engineering enhanced thermal conductivity in GSHE installations is best-practice, even increasing λ by the application of irrigation has been proposed as a cost effective alternative to using larger loops.[9] The left-skewed frequency distributions of λ at all depths in the lysimeter (See Figs. 9e to 9h) indicate the ability for SuDS to remain in a higher thermal conductivity range, even in summer, which eliminates any need for temporary, artificial modification of ground conditions such as irrigation.

5. Conclusions

Using an at-scale experimental setup, this work has demonstrated that the thermo-hydrological conditions within an engineered SuDS are conducive to efficient ground heat exchange. SuDS, and Green Infrastructure in general, are principally incorporated into the urban environment to manage excess surface water, this study has shown how these systems maintain high thermal conductivity states, even under summer conditions. The monitored soil-water-atmosphere interaction, assessed in combination with a comprehensive campaign of saturated-unsaturated laboratory testing, has illustrated the highly thermo-hydrologically coupled response of a functioning SuDS. Insight has been presented into the TCDC performance of the SuDS substrate under laboratory conditions and compared to that measured in the field. An improved understanding of the implications of TCDCs for GSHE-SuDS design has been established. Such co-located systems have the potential for significant mutual benefit in terms of environmental and economic performance, leading to a more attractive proposition for sustainable water-energy approaches in urban environments.

CRediT authorship contribution statement

Acknowledgements

References

1. Fleiter T, Herbst A, Hirzel S, et al. *Mapping and Analyses of the Current and Future (2020 - 2030) Heating/Cooling Fuel Deployment (Fossil/Renewables) - Work Package 1: Final Energy Consumption for the Year 2012.*; 2017. https://ec.europa.eu/energy/en/studies/mapping-and-analyses-current-and-future-2020-2030-heatingcooling-fuel-deployment.
2. Younger P. Geothermal Energy: Delivering on the Global Potential. *Energies*. 2015;8(10):11737-11754. doi:10.3390/en81011737
3. Sarbu I, Sebarchievici C. General review of ground-source heat pump systems for heating and cooling of buildings. *Energy Build*. 2014;70:441-454. doi:10.1016/j.enbuild.2013.11.068
4. Rybach L, Sanner B. Ground-source heat pump systems - the European Experience. *GHC Bull*. 2000:16-26.
5. Chalhoub M, Bernier M, Coquet Y, Philippe M. A simple heat and moisture transfer model to predict ground temperature for shallow ground heat exchangers. *Renew Energy*. 2017;103:295-307. doi:10.1016/j.renene.2016.11.027
6. Di Sipio E, Bertermann D. Factors influencing the thermal efficiency of horizontal ground heat exchangers. *Energies*. 2017;10(11). doi:10.3390/en10111897
7. Busby J. Determination of Thermal Properties for Horizontal Ground Collector Loops. In: *Proceedings World Geothermal Congress*. Melbourne, Australia; 2015.
8. Dalla Santa G, Galgaro A, Sassi R, et al. An updated ground thermal properties database for GSHP applications. *Geothermics*. 2020;85:101758. doi:10.1016/j.geothermics.2019.101758
9. Naylor S, Ellett KM, Gustin AR. Spatiotemporal variability of ground thermal properties in glacial sediments and implications for horizontal ground heat exchanger design. *Renew Energy*. 2015;81:21-30. doi:10.1016/j.renene.2015.03.006
10. Congedo PM, Colangelo G, Starace G. CFD simulations of horizontal ground heat

exchangers: A comparison among different configurations. *Appl Therm Eng*. 2012;33-34:24-32. doi:10.1016/j.applthermaleng.2011.09.005

11. Wu R, Tinjum JM, Likos WJ. Coupled Thermal Conductivity Dryout Curve and Soil–Water Characteristic Curve in Modeling of Shallow Horizontal Geothermal Ground Loops. *Geotech Geol Eng*. 2015;33(2):193-205. doi:10.1007/s10706-014-9811-2

12. Chong CSA, Gan G, Verhoef A, Garcia RG, Vidale PL. Simulation of thermal performance of horizontal slinky-loop heat exchangers for ground source heat pumps. *Appl Energy*. 2013;104:603-610. doi:10.1016/j.apenergy.2012.11.069

13. Woods Ballard B, Wilson S, Udale-Clarke H, et al. *The SUDS Manual*. CIRIA; 2015. http://www.persona.uk.com/A47postwick/deposit-docs/DD-181.pdf.

14. Charlesworth SM, Faraj-Llyod AS, Coupe SJ. Renewable energy combined with sustainable drainage: Ground source heat and pervious paving. *Renew Sustain Energy Rev*. 2017;68:912-919. doi:10.1016/j.rser.2016.02.019

15. Rey-Mahía C, Sañudo-Fontaneda LA, Andrés-Valeri VC, Álvarez-Rabanal FP, Coupe SJ, Roces-García J. Evaluating the thermal performance ofwet swales housing ground source heat pump elements through laboratory modelling. *Sustain*. 2019;11(11). doi:10.3390/su11113118

16. Salager S, Rizzi M, Laloui L. An innovative device for determining the soil water retention curve under high suction at different temperatures. *Acta Geotech*. 2011;6(3):135-142. doi:10.1007/s11440-011-0141-8

17. Le Fevre GH, Paus KH, Natarajan P, Gulliver JS, Novak PJ, Hozalski RM. Review of dissolved pollutants in urban storm water and their removal and fate in bioretention cells. *J Environ Eng (United States)*. 2015;141(1). doi:10.1061/(ASCE)EE.1943-7870.0000876

18. The European Parliament and the Council of European Union. *Directive 2000/60/EC*.; 2000. https://eur-lex.europa.eu/legal-content/EN/TXT/?uri=CELEX:02000L0060-20141120.

19. UK Public General Acts. *Flood and Water Management Act*.; 2010. http://www.legislation.gov.uk/ukpga/2010/29/contents.

20. Ministry of Housing C& LG. *National Planning Policy Framework*.; 2019.

21. HM Treasury. *Spring Statement 2019: Written Ministerial Statement*.; 2019. https://assets.publishing.service.gov.uk/government/uploads/system/uploads/attachment_data/file/785618/WMS_final_Commons.pdf.

22. Meter Group. KSAT. https://www.metergroup.com/app/uploads/2018/12/KSAT_Manual.042019.pdf. Accessed February 5, 2020.

23. DWA German Association for Water W and W. Standard DWA-A 138E Planning, Construction and Operation of Facilities for the Percolation of Precipitation Water. 2005.

24. Toronto and Region Conservation Authority. *Low Impact Development Stormwater Management Planning and Design Guide*.; 2010.

25. North Carolina Department for Environmental Quality. Stormwater Design Manual. https://deq.nc.gov/sw-bmp-manual. Published 2017. Accessed April 22, 2020.

26. Payne E, Hatt B, Deletic A, Dobbie M, McCarthy D, Charasena G. *Adoption Guidelines for Stormwater Biofiltration Systems Cities as Water Supply Catchments*.; 2015.

27. New Jersey Department of Environmental Protection. NJ Stormwater Best Management Practices Manual. https://www.njstormwater.org/bmp_manual2.htm. Published 2018. Accessed April 22, 2020.

28. Green-tech. Green-Tree Topsoil. https://www.green-tech.co.uk/media/shared/data-sheets/2018-green-tree/Green-tree-Top-Soil-Green-tree.pdf. Accessed October 29, 2019.

29. Department for Environment F and RA. *The Impact of Subsoil Compaction on Soil Functionality & Landscape*. Bristol, UK; 2006.

30. Mårtensson LM. Methods of establishing species-rich meadow biotopes in urban areas. *Ecol Eng*. 2017;103:134-140. doi:10.1016/j.ecoleng.2017.03.016

31. Cuaran A, Lundberg L, Holmberg J. Design of Bioretention Planters for Stormwater Flow Control and Removal of Toxic Metals and Organic Contaminants. *Dep Energy Environ*. 2015. http://publications.lib.chalmers.se/records/fulltext/225206/225206.pdf.

32. Meter Group. HYPROP. http://library.metergroup.com/Manuals/18263_HYPROP_Manual_Web.pdf. Published 2019. Accessed November 22, 2019.

33. Decagon Devices Inc. KD2 Pro Thermal Properties Analyzer. 2016. http://manuals.decagon.com/Manuals/13351_KD2 Pro_Web.pdf. Accessed April 21, 2020.

34. Johansen O. Thermal Conductivity of Soils. 1975.

35. Tarnawski VR, Leong WH. Advanced Geometric Mean Model for Predicting Thermal Conductivity of Unsaturated Soils. *Int J Thermophys*. 2016;37(2):18. doi:10.1007/s10765-015-2024-y

36. Zhang M, Bi J, Chen W, Zhang X, Lu J. Evaluation of calculation models for the thermal conductivity of soils. *Int Commun Heat Mass Transf*. 2018;94(March):14-23. doi:10.1016/j.icheatmasstransfer.2018.02.005

37. Lu S, Ren T, Gong Y, Horton R. An Improved Model for Predicting Soil Thermal Conductivity from Water Content at Room Temperature. *Soil Sci Soc Am J*. 2007;71(1):8-14. doi:10.2136/sssaj2006.0041

38. Brigaud F, Vasseur G. Mineralogy, porosity and fluid control on thermal conductivity of sedimentary rocks. *Geophys J Int*. 1989;98(3):525-542. doi:10.1111/j.1365-246X.1989.tb02287.x

39. He H, Zhao Y, Dyck MF, et al. A modified normalized model for predicting effective soil thermal conductivity. *Acta Geotech*. 2017;12(6):1281-1300. doi:10.1007/s11440-017-0563-z

40. Côté J, Konrad J-M. Thermal conductivity of base-course materials. *Can Geotech J*. 2005;42:61-78. doi:10.1139/t04-081

41. Meter Group. Meter Group Retired and Discontinued Product Manuals. http://library.metergroup.com/Retired and Discontinued/Manuals/. Published 2019. Accessed June 19, 2019.

42. Hukseflux Thermal Sensors BV. TP01 User Manual. https://www.hukseflux.com/uploads/product-documents/TP01_manual_v1627.pdf. Accessed March 31, 2020.

43. Yildiz A, Stirling RA. PLEXUS @ NGIF - Field and laboratory measurements. doi:10.25405/data.ncl.c.5088419

44. Yildiz A. Data analysis and visualisation for lysimeter data. https://github.com/yildizanil/GETE-D-20-00044. Published 2020. Accessed July 20, 2020.

45. van Genuchten MT. A closed-form equation for predicting the hydraulic conductivity of unsaturated soils. *Soil Sci Soc Am J*. 1980;44:892-898.

46. Yildiz A. Estimating the full range of thermal conductivity dryout curve. *Géotechnique Lett*. 2020;10(3):1-13. doi:10.1680/jgele.20.00055

47. Allen RG, Pereira LS, Raes D, Smith M. *FAO Irrigation and Drainage Paper No. 56 - Crop Evapotranspiration*.; 1998.

48. Kozak JA, Ahuja LR, Green TR, Ma L. Modelling crop canopy and residue rainfall interception effects on soil hydrological components for semi-arid agriculture. *Hydrol*

Process. 2007;21(2):229-241. doi:10.1002/hyp.6235

49. Kołodziej J. Rainfall Interception by Cultivated Plants. In: Gliński J, Horabik J, Lipiec J, eds. *Encyclopedia of Agrophysics*. Dordrecht: Springer Netherlands; 2011:679-681. doi:10.1007/978-90-481-3585-1_253

50. Cassel DK, Nielsen DR. Field Capacity and Available Water Capacity. In: Klute A, ed. *Methods of Soil Analysis: Part 1 Physical and Mineralogical Methods*. ; 1986:901-926. doi:10.2136/sssabookser5.1.2ed.c36

51. Chen Y. Soil–Water Retention Curves Derived as a Function of Soil Dry Density. *GeoHazards*. 2018;1(1):3-19. doi:10.3390/geohazards1010002

52. Schindler U, Durner W, von Unold G, Müller L. Evaporation Method for Measuring Unsaturated Hydraulic Properties of Soils: Extending the Measurement Range. *Soil Sci Soc Am J*. 2010;74(4):1071-1083. doi:10.2136/sssaj2008.0358

53. Degré A, van der Ploeg MJ, Caldwell T, Gooren HPA. Comparison of Soil Water Potential Sensors: A Drying Experiment. *Vadose Zo J*. 2017;16(4):vzj2016.08.0067. doi:10.2136/vzj2016.08.0067

54. Oorthuis R, Hürlimann M, Fraccica A, et al. Monitoring of a full-scale embankment experiment regarding soil–vegetation–atmosphere interactions. *Water*. 2018;10:688. doi:10.3390/w10060688

55. Likos WJ. Modeling thermal conductivity dryout curves from soil-water characteristic curves. *J Geotech Geoenvironmental Eng*. 2014;140(5):1-13. doi:10.1061/(ASCE)GT.1943-5606.0001078

56. Smits KM, Sakaki T, Limsuwat A, Illangasekare TH. Thermal Conductivity of Sands under Varying Moisture and Porosity in Drainage–Wetting Cycles. *Vadose Zo J*. 2010;9(1):172. doi:10.2136/vzj2009.0095

57. Wang X, Yu X, Kaneza N, He S. Measurement of Thermal Conductivity Dryout and SWCC Curves for Sands Using a Modified Hanging Column Device. *Geotech Spec Publ*. 2019;2019-March(GSP 310):794-803. doi:10.1061/9780784482124.080

58. Tarnawski VR, Momose T, McCombie ML, Leong WH. Canadian Field Soils III. Thermal-Conductivity Data and Modeling. *Int J Thermophys*. 2015;36(1):119-156. doi:10.1007/s10765-014-1793-z

59. Udukumburage RS, Gallage C, Dawes L. An instrumented large soil column to investigate climatic ground interaction. *Int J Phys Model Geotech*. 2020;(Paper 1900007):1-17. doi:10.1680/jphmg.19.00007

60. Nikolaev I V., Leong WH, Rosen MA. Experimental investigation of soil thermal conductivity over a wide temperature range. *Int J Thermophys*. 2013;34(6):1110-1129. doi:10.1007/s10765-013-1456-5

61. Dong Y, Lu N, Wayllace A, Smits K. Measurement of thermal conductivity function of unsaturated soil using a transient water release and imbibition method. *Geotech Test J*. 2014;37(6). doi:10.1520/GTJ20140046

62. Tarnawski VR, Leong WH. Thermal conductivity of soils at very low moisture content and moderate temperatures. *Transp Porous Media*. 2000;41(2):137-147. doi:10.1023/A:1006738727206

63. Ghanbarian B, Daigle H. Thermal conductivity in porous media: Percolation-based effective-medium approximation. *Water Resour Res*. 2016;52(1):295-314. doi:10.1002/2015WR017236